Multiconverter System Design for Fuel Cell Buffering and Diagnostics Under UAV Load Profiles

John J. Cooley, *Member, IEEE*, Peter Lindahl, *Student Member, IEEE*, Clarissa L. Zimmerman, Matthew Cornachione, Grant Jordan, Steven R. Shaw, *Senior Member, IEEE*, and Steven B. Leeb, *Fellow, IEEE*

***Abstract*—This paper presents a multisource, multiconverter power system for electrically propelled unmanned aerial vehicles (UAVs) with a focus on promoting fuel cell health. Linearized multiconverter system analysis and the two extra element theorem (2EET) inform a system design for fuel cell current buffering and integral diagnostics. Integral diagnostics is *in situ* impedance spectroscopy achieved by controlling the power system to superpose a frequency-swept excitation current at the fuel cell terminals. An experimental system demonstrates hybridization of a solid-oxide fuel cell (SOFC) with a lead-acid battery having suitable current buffering and integral diagnostics performance under UAV load profiles. Experimental behavior is demonstrated with an electrically emulated SOFC stack or "reference simulator." Impedance spectroscopy data measured during run-time clearly indicate both degradation and recovery phenomena in the SOFC.**

***Index Terms*—Battery, extra element theorem, fuel cell, hybrid, input filter, Middlebrook, multiconverter, multisource, unmanned aerial vehicle (UAV).**

I. Introduction

THE practice of combining power sources is increasingly necessitated for solving problems of scale. Multisource or hybrid power systems are recently popular for achieving critical tradeoffs in mobility applications [1]–[8] and grid level power applications [1], [5], [9]–[11]. Fuel cells are a particularly interesting candidate for hybridization in these applications because they offer relatively clean, high-efficiency conversion of high-energy density fuels but are limited by durability issues that may be related to and therefore addressed through electrical power conditioning [6], [11]–[13].

Fuel cell hybridization solutions generally employ a second power source for sufficient additional degrees of freedom to support continuous operation near the fuel cell's optimum power level [4]–[6], [11], [13], [14]. Meanwhile, multiconverter systems, especially feedback regulated multiconverter systems, present design challenges not addressed by single converter design methodologies [1], [3], [5], [6], [15]–[18]. Multiconverter design methodologies have historically relied on linearized modeling of switched-mode converters and extensions of linear system theory as applied to single converter systems [19]–[21]. The linearized converter modeling in this paper relies closely on previous work developed by Middlebrook [22].

This paper explores the aspects of feedback control design and linearized converter modeling to address hybridized fuel cell systems in mobility applications. Specifically, this paper focuses on methods to implement integral diagnostics in a multiconverter power system by way of impedance spectroscopy signals generated by injection of control signals to the feedback control loops in the converters themselves. Interesting design challenges are addressed including load disturbance during impedance spectroscopy, and power converter input filter design. Careful input filter design is unusually critical in this application, so this paper employs Middlebrook's 2-Extra Element Theorem (2EET) to inform tradeoffs between loop stability and transmission of impedance spectroscopy current to the fuel cell terminals [23].

The experimental power system is demonstrated for use in an electrically propelled unmanned aerial vehicle (UAV) application. Experimental behavior is demonstrated with an electrically emulated solid-oxide fuel cell (SOFC) stack or "reference simulator." The reference simulator uses a single SOFC fuel cell and an electronic amplifier to emulate the behavior of a stack of cells. The power system is loaded with an electronic load generating profiles taken from an actual UAV.[1] Impedance spectroscopy data taken from the multiconverter system further demonstrate an interesting phenomenon in which a fuel cell is first shown to degrade and to subsequently recover in response to electrical loading.

Section II presents the linearized multiconverter system model and Section III evaluates the system in an example closed-loop configuration. Section IV investigates the effect of adding input filters to both converters. Finally, Section V presents an experimental system and SOFC impedance spectroscopy results.

Manuscript received January 5, 2013; revised June 1, 2013; accepted July 8, 2013. Date of current version January 29, 2014. Recommended for publication by Associate Editor S. Choi.

J. J. Cooley is with the FastCAP Systems Inc., Boston, MA 02210 USA (e-mail: cooleymobile@gmail.com).

P. Lindahl is with Blackmore Energy, LLC, Bozeman MT 59717 USA (e-mail: petelindahl@gmail.com).

C. L. Zimmerman and S. B. Leeb are with the Massachusetts Institute of Technology Cambridge, MA 02139 USA (e-mail: clzimmer@mit.edu; sbleeb@mit.edu).

M. Cornachione is with the Rocky Mountain Power, Salt Lake City, UT 84111 USA (e-mail: mcornach@gmail.com).

G. Jordan is with the University of California San Diego, San Diego, CA 92093 USA (e-mail: Grant.Jordan@wpafb.af.mil).

S. R. Shaw is with the Department of Electrical and Computer Engineering, Montana State University Bozeman, MT 59717 USA (e-mail: sshaw@matrix.coe.montana.edu).

Color versions of one or more of the figures in this paper are available online at http://ieeexplore.ieee.org.

Digital Object Identifier 10.1109/TPEL.2013.2274600

[1]Data used in the experiments made available by the USAF has been cleared for public release.

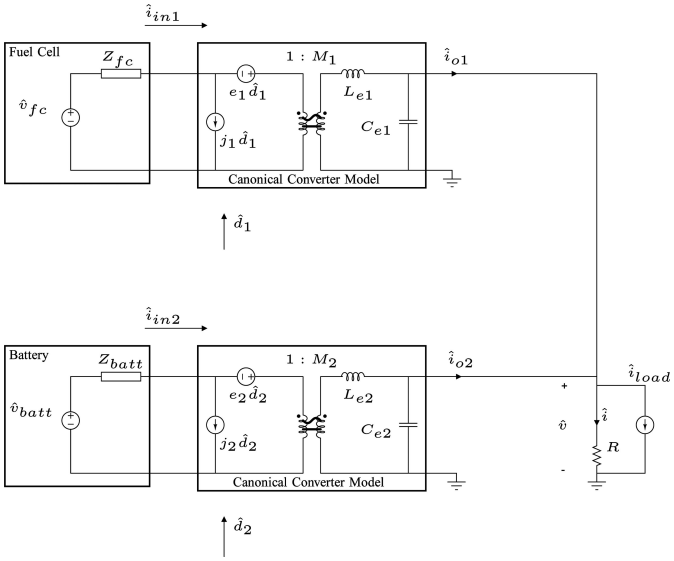

Fig. 1. Linearized multiconverter system model.

II. Linearized Multiconverter System Model

The system model in Fig. 1 is a starting point for the analysis and design of the multiconverter regulator in this paper. It is the circuit used to derive the transfer functions from independent inputs to dependent outputs in the unregulated power system (converter transfer functions).

By leaving the system model in terms of the canonical converter model parameters, the mathematical results derived from it may be applied to any converter topology, e.g., buck, boost, or buck–boost. Cooley in [24] summarizes some example model parameters generalized from single-converter results.

The block diagram in Fig. 2 represents a linear superposition of the effects of the converter transfer functions. The linear superposition expressions may be written directly, for instance, the load voltage is

$$\hat{v}(\hat{d}_1, \hat{d}_2, \hat{i}_{\rm load}) = \left(\frac{\hat{v}}{\hat{d}_1}\right)\hat{d}_1 + \left(\frac{\hat{v}}{\hat{d}_2}\right)\hat{d}_2 + \left(\frac{\hat{v}}{\hat{i}_{\rm load}}\right)\hat{i}_{\rm load} \quad (1)$$

where hatted ($\wedge$) quantities are small-signal quantities describing operation of a linearized power converter, v is the load voltage, $\hat{d}_1$ and $\hat{d}_2$ are the duty ratios of the first and second converters, and $\hat{i}_{\rm load}$ is the load current. The quantities in parentheses in (1), and in the blocks in Fig. 2, are the converter transfer functions. The derivation of the converter transfer functions is left to [24]. The first converter's input current will be important in Section V. It can be found from KCL in Fig. 1

$$\hat{i}_{\rm in1}(\hat{d}_1, \hat{d}_2) = j_1\hat{d}_1 + M_1\left(\hat{i}_{o1}(\hat{d}_1, \hat{d}_2) + \frac{\hat{v}(\hat{d}_1, \hat{d}_2)}{Z_{\rm ce1}}\right) \quad (2)$$

where $\hat{i}_{\rm in1}$ is the first converter's input current, j_1 is a linearized model parameter corresponding to input current generation, M_1 is a linearized model parameter corresponding to the ideal conversion ratio, and $Z_{\rm ce1}$ is the impedance of the first converter's effective open-loop output capacitance. Additional derivations can be found in [24].

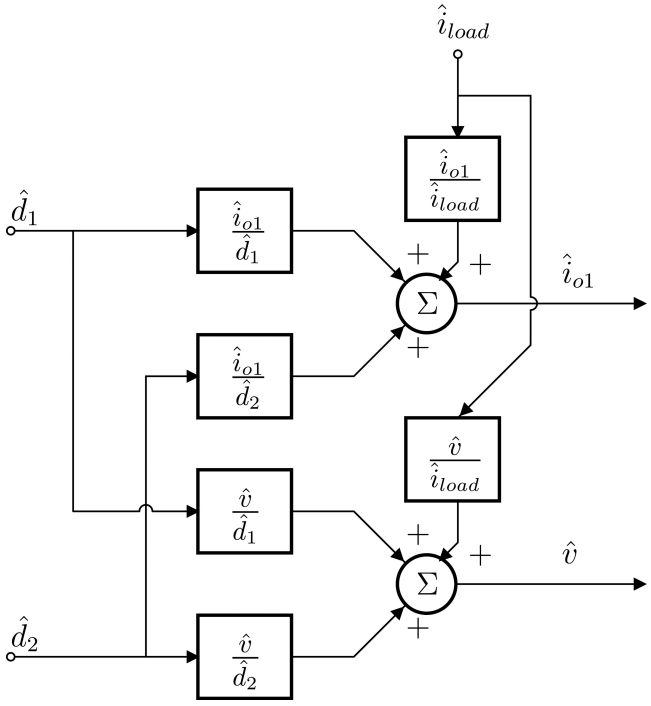

Fig. 2. Block diagram representation of the mathematical relations governing the circuit in Fig. 1.

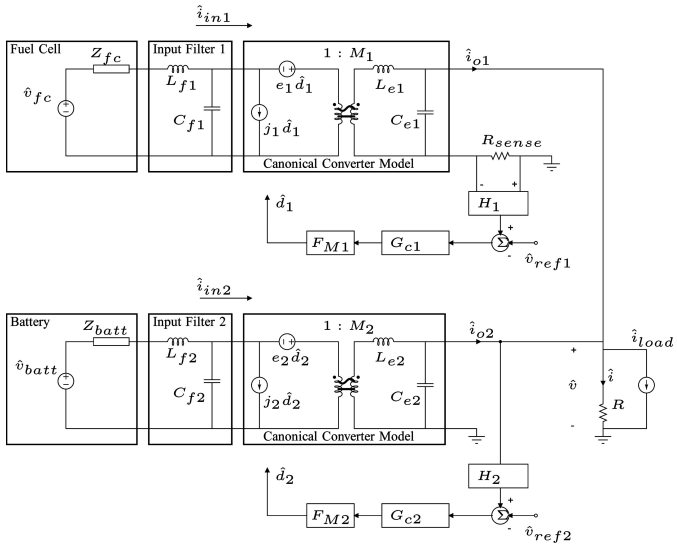

Fig. 3. Current–voltage regulator linearized system model.

III. Example Closed Loop System: Current–Voltage Regulator

In Fig. 3, the system model is coupled to a feedback control system to form a regulator. This example considers two power converters, one load voltage regulated and the other output current regulated—a useful configuration for load sharing and also useful for achieving the design goals listed in the Introduction. Fig. 4 shows the corresponding block diagram representation. It comprises the block diagram from Fig. 2 and additional blocks representing a feedback control system. The $\times$'s are points to break in the block diagram to evaluate open-loop transfer

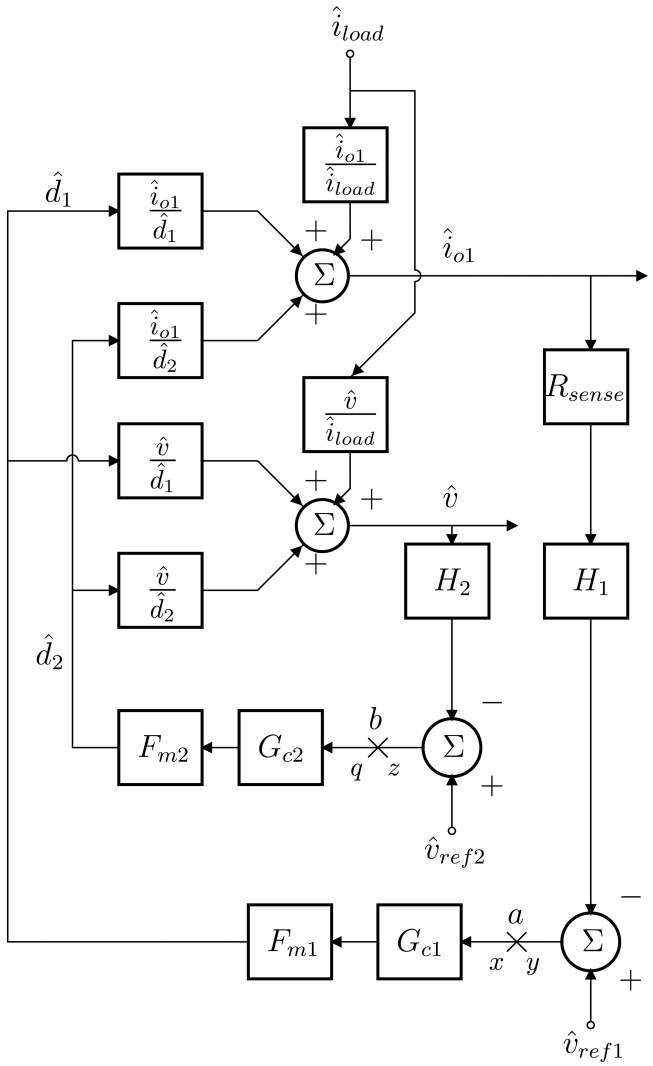

Fig. 4. Block diagram representation of the mathematical relations governing the circuit in Fig. 3.

functions. The input filters are ignored until Section IV. (The inductors $L_{f1,2}$ are shorted and the capacitors $C_{f1,2}$ are open.)

A. Closed-Loop Transfer Functions

We will use the direct evaluation of closed-loop transfer functions to evaluate the design of the experimental system regarding the design goals listed in the Introduction. To that end, we consider the system in Figs. 3 and 4 in which $\hat{v}_{\rm ref1}$ is designated the "control signal" (to control the first converter to generate an excitation current for impedance spectroscopy of the fuel cell), while the other small signal reference voltage is deactivated. For the following analyses, refer to Figs. 3 and 4 for variable definitions. The two duty ratios become

$$\hat{d}_1 = F_{m1}G_{c1}\left(\hat{v}_{\rm ref1} - H_1 R_{\rm sense}\hat{i}_{o1}\right) \tag{3}$$

and

$$\hat{d}_2 = -F_{m2}G_{c2}H_2\hat{v}. \tag{4}$$

Some interesting closed-loop transfer functions may be written as linear decompositions as follows. The notation $|_{\rm CL}$ used here denotes a closed-loop transfer function. Rewriting the effects of the summing junctions in Fig. 4 (and deactivating $\hat{i}_{\rm load}$), the transfer function from the control signal to the load voltage is

$$\left.\frac{\hat{v}}{\hat{v}_{\rm ref1}}\right|_{\rm CL} = \frac{\hat{v}}{\hat{d}_1}\frac{\hat{d}_1}{\hat{v}_{\rm ref1}} + \frac{\hat{v}}{\hat{d}_2}\frac{\hat{d}_2}{\hat{v}_{\rm ref1}} \tag{5}$$

and the transfer function from the control signal to the first converter's output current is

$$\left.\frac{\hat{i}_{o1}}{\hat{v}_{\rm ref1}}\right|_{\rm CL} = \frac{\hat{i}_{o1}}{\hat{d}_1}\frac{\hat{d}_1}{\hat{v}_{\rm ref1}} + \frac{\hat{i}_{o1}}{\hat{d}_2}\frac{\hat{d}_2}{\hat{v}_{\rm ref1}}. \tag{6}$$

Re-solving the circuit in Fig. 3, the first converter's input current response to the control signal is

$$\left.\frac{\hat{i}_{\rm in1}}{\hat{v}_{\rm ref1}}\right|_{\rm CL} = j_1\frac{\hat{d}_1}{\hat{v}_{\rm ref1}} + M_1\left(\left.\frac{\hat{i}_{o1}}{\hat{v}_{\rm ref1}}\right|_{\rm CL} + \left.\frac{\hat{v}}{\hat{v}_{\rm ref1}}\right|_{\rm CL}\frac{1}{Z_{ce1}}\right). \tag{7}$$

Writing the closed-loop transfer functions this way separates them into converter transfer functions, which may have already been derived according to Section II, and transfer functions that may be found from the block diagram representation in Fig. 4. Analyzing the block diagram in Fig. 4 yields the terms needed to complete the closed-loop transfer functions above

$$\frac{\hat{d}_1}{\hat{v}_{\rm ref1}} = \frac{F_{m1}G_{c1}}{\alpha}\left(1 + \frac{F_{m1}G_{c1}H_1R_{\rm sense}\frac{\hat{i}_{o1}}{\hat{d}_2}\frac{\hat{d}_2}{\hat{d}_1}}{\alpha}\right)^{-1} \tag{8}$$

and

$$\frac{\hat{d}_2}{\hat{v}_{\rm ref1}} = \frac{\hat{d}_1}{\hat{v}_{\rm ref1}}\frac{\hat{d}_2}{\hat{d}_1} \tag{9}$$

where

$$\frac{\hat{d}_2}{\hat{d}_1} = -\frac{H_2F_{m2}G_{c2}\frac{\hat{v}}{\hat{d}_1}}{1 + H_2F_{m2}G_{c2}\frac{\hat{v}}{\hat{d}_2}} \tag{10}$$

and we define

$$\alpha \equiv 1 + F_{m1}G_{c1}H_1R_{\rm sense}\frac{\hat{i}_{o1}}{\hat{d}_1}. \tag{11}$$

The same analytical approach can be used to find the closed-loop transfer functions from the load current $\hat{i}_{\rm load}$ to the output signals of interest, $\hat{v}, \hat{i}_{o1}$, and $\hat{i}_{\rm in1}$. Those details are left to [24].

Several important system characteristics can be gleaned directly from expressions for the closed-loop transfer functions. For instance, as the voltage feedback gain, G_{c2}, increases toward ∞, the ratio $\frac{\hat{d}_2}{\hat{d}_1}$ approaches -1. The control signal has the opposite effect on the two converter duty ratios suggesting the manner in which the voltage regulated converter counteracts perturbations of the opposite converter's behavior, stabilizes the load voltage, and absorbs excess current arising from impedance spectroscopy. Meanwhile, in [24], we show that as the current feedback gain G_{c1} increases toward ∞, the collapse of the closed-loop transfer function from load current variations to the first converter's input current (in other words, good fuel

cell current buffering) is only valid at zero frequency if we take into account nonzero resistive impedance present in the first converter's output network, e.g., inductor and capacitor ESR, and current sense resistance.

B. Open-Loop Transfer Functions

The open-loop transfer functions are useful for studying system stability. To evaluate them, we can break the loops at the $\times$'s and consider the signals that return when injecting a signal into the break. Mathematically, the loop transfer functions of interest are

$$T_1 = -\frac{y}{x} \tag{12}$$

$$T_2 = -\frac{z}{q}. \tag{13}$$

In the case of one voltage and one current feedback loop, these transfer functions are

$$T_1 = H_1 R_{\text{sense}} \frac{\hat{i}_{o1}}{x} \tag{14}$$

$$T_2 = H_2 \frac{\hat{v}}{q}. \tag{15}$$

Expanding the measured signals, $\hat{v}$ and $\hat{i}_{o1}$, using linear signal decomposition, the transfer functions become

$$T_1 = H_1 R_{\text{sense}} \left(\frac{\hat{d}_2}{x} \frac{\hat{i}_{o1}}{\hat{d}_2} + \frac{\hat{d}_1}{x} \frac{\hat{i}_{o1}}{\hat{d}_1} \right) \tag{16}$$

$$T_2 = H_2 \left(\frac{\hat{d}_1}{q} \frac{\hat{v}}{\hat{d}_1} + \frac{\hat{d}_2}{q} \frac{\hat{v}}{\hat{d}_2} \right). \tag{17}$$

The loop transfer function T_2 corresponds to the voltage feedback loop evidenced by the converter transfer functions that it depends on most directly and by the error signal that it corresponds to in the block diagram of Fig. 4. Similarly, the loop transfer function T_1 corresponds to the current feedback loop. Breaking the loop at point a and solving leads to the needed inner transfer functions for expressing T_1

$$\frac{\hat{d}_1}{x} = G_{c1} F_{m1} \tag{18}$$

$$\frac{\hat{d}_2}{x} = -\frac{F_{m2} G_{c2} H_2 G_{c1} F_{m1} \frac{\hat{v}}{\hat{d}_1}}{1 + F_{m2} G_{c2} H_2 \frac{\hat{v}}{\hat{d}_2}}. \tag{19}$$

Breaking the loop at point b and solving leads to the needed inner transfer functions for expressing T_2

$$\frac{\hat{d}_1}{q} = G_{c1} F_{m1} \tag{20}$$

$$\frac{\hat{d}_2}{q} = -\frac{F_{m1} G_{c1} H_1 R_{\text{sense}} F_{m2} G_{c2} \frac{\hat{i}_{o1}}{\hat{d}_2}}{1 + F_{m1} G_{c1} H_1 R_{\text{sense}} \frac{\hat{i}_{o1}}{\hat{d}_1}}. \tag{21}$$

The remaining terms in (16) and (17) can be recognized as converter transfer functions, which may have already been derived according to Section II.

IV. Multiple Input Filters in Multiconverter, Multisource Power Systems

"Although it would be unlikely that one would want to modify a transfer function to account simultaneously for two previously unrecognized extra elements, there is considerable potential advantage to be obtained from a Low-Entropy Expression for a transfer function in which the influences of two designated elements are directly exposed, in terms of their [driving point impedances]."

—R.D. Middlebrook, The Two Extra Element Theorem [23]

The hybrid power system is an example where the "two extra element" theorem is helpful for design and analysis. So far, our analyses of the multi-converter system have assumed ideal input sources—those having zero-valued output impedances. Typical requirements for practical designs specify a maximum amount of input current ripple. An input filter is often needed to meet these requirements. However, the addition of an input filter modifies the effective source impedance presented to the converter. The designer must know how to select input filter components, so that the ideal input source assumption that was implicit in the converter design is not significantly undermined. In this section, we extend Middlebrook's application of the extra element theorem to "account simultaneously for two previously unrecognized extra elements" (input filters) in a multiconverter, multisource power system.

A. 2EET for Multiple Input Filter Evaluation

In [23], Middlebrook presents the 2EET, the principle result of which is the correction factor for the i^{th} transfer function

$$\text{CF}^{(i)} = \frac{1 + \frac{Z_1}{Z_{N1}|^{(i)}_{Z_2=0}} + \frac{Z_2}{Z_{N2}|^{(i)}_{Z_1=0}} + K_N^{(i)} \frac{Z_1 Z_2}{Z_{N1}|^{(i)}_{Z_2=0} Z_{N2}|^{(i)}_{Z_1=0}}}{1 + \frac{Z_1}{Z_{D1}|^{(i)}_{Z_2=0}} + \frac{Z_2}{Z_{D2}|^{(i)}_{Z_1=0}} + K_D^{(i)} \frac{Z_1 Z_2}{Z_{D1}|^{(i)}_{Z_2=0} Z_{D2}|^{(i)}_{Z_1=0}}} \tag{22}$$

where Z_1 and Z_2 are the output impedances of the first and second input filters, respectively. The subscripts N and D historically represent "numerator" and "denominator" [25]. In (22), impedances with an N subscript are the null-condition impedances while those with a D subscript are the open-loop impedances. The superscripts (i) indicate the transfer function for which the special-case impedances are derived. The interaction parameters can be written (they each have two possible forms) [23]

$$K_N^{(i)} = \frac{Z_{N1}|^{(i)}_{Z_2=0}}{Z_{N1}|^{(i)}_{Z_2=\infty}} = \frac{Z_{N2}|^{(i)}_{Z_1=0}}{Z_{N2}|^{(i)}_{Z_1=\infty}} \tag{23}$$

$$K_D^{(i)} = \frac{Z_{D1}|^{(i)}_{Z_2=0}}{Z_{D1}|^{(i)}_{Z_2=\infty}} = \frac{Z_{D2}|^{(i)}_{Z_1=0}}{Z_{D2}|^{(i)}_{Z_1=\infty}}. \tag{24}$$

For the i^{th} open-loop transfer function, there are four special-case impedances shown explicitly in the expression for the corresponding correction factor (22): $Z_{N1}|^{(i)}_{Z_2=0}$, $Z_{N2}|^{(i)}_{Z_1=0}$, $Z_{D1}|^{(i)}_{Z_2=0}$, and $Z_{D2}|^{(i)}_{Z_1=0}$. Additionally, two more special-case impedances are required to calculate the interaction parameters,

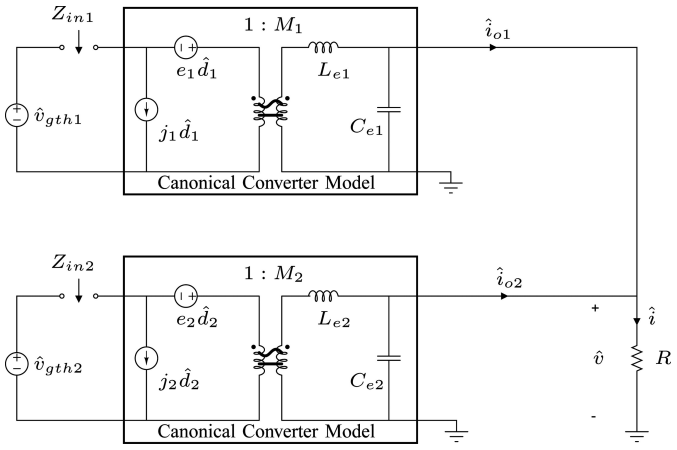

Fig. 5. Circuit used for calculating the special-case impedances for the 2EET correction factors.

$K_N^{(i)}$ and $K_D^{(i)}$ as shown in (23) and (24), for a total of six special-case impedances. The converter transfer functions may be corrected by multiplying by the corresponding correction factor. Those converter transfer functions that are "in the loop" will carry the effect of the correction factor to the loop transfer functions and will impact the stability of the closed-loop system.

The expression for the correction factor in (22) suggests that the i^{th} open-loop converter transfer function will not be impacted significantly if the following impedance inequalities are met

$$|Z_1| \ll |\, Z_{N1}|_{Z_2=0}^{(i)}\,| \tag{25}$$

$$|Z_2| \ll |\, Z_{N2}|_{Z_1=0}^{(i)}\,| \tag{26}$$

$$|Z_1| \ll |\, Z_{D1}|_{Z_2=0}^{(i)}\,| \tag{27}$$

$$|Z_2| \ll |\, Z_{D2}|_{Z_1=0}^{(i)}\,|. \tag{28}$$

Note that meeting these impedance qualities may be sufficient but not necessary to preserve the stability of an otherwise stable regulated power system. Naturally, the 2EET dictates that the input filter output impedances should generally be small in order to preserve the low impedance aspect of the source.

B. Example: Correction Factor for $\hat{v}/\hat{d}_1$ in a Hybrid Power System

The circuit used for analysis in this section is shown in Fig. 5. The independent inputs in that system include the duty ratios for the two converters, $\hat{d}_1$ and $\hat{d}_2$, as well as their (Thevenin) input voltages, $\hat{v}_{g\text{th}1}$ and $\hat{v}_{g\text{th}2}$. Deactivating one of the duty ratio signals shorts the corresponding $e\hat{d}$ source and opens the corresponding $j\hat{d}$ source in that converter model. In analyzing each transfer function, defined by an independent input and a corresponding output, all other independent inputs are deactivated resulting in a circuit that is a simplified version of the one in Fig. 5. The following quantities are defined. The impedance Z_L is all of the impedance that shunts the output node, $Z_L \equiv R \| Z_{\text{ce}1} \| Z_{\text{ce}2}$ and the effective converter output impedances are $Z_{e1} \equiv Z_{\text{le}1} \| Z_{\text{ce}1}$ and $Z_{e2} \equiv Z_{\text{le}2} \| Z_{\text{ce}2}$, where $Z_{\text{ce}1,2} \equiv 1/sC_{e1,2}$ and $Z_{\text{le}1,2} \equiv sL_{e1,2}$.

Designating $\hat{v}/\hat{d}_1$ as the first transfer function, the superscripts for the six special-case impedances are all (1). The other independent inputs, $\hat{d}_2$, $\hat{v}_{g\text{th}1}$ and $\hat{v}_{g\text{th}2}$, are all deactivated leading to some simplification of the circuit in Fig. 5. For instance, the first special-case impedance $Z_{N1}|_{Z_2=0}^{(1)}$ is the null-condition impedance at the first extra element port with the second extra element port shorted. Because it is a null-condition impedance, analysis of the circuit should address the fact that the independent input in this transfer function $\hat{d}_1$ will be directed such that the output voltage $\hat{v}$ is nulled. With this condition, and with the other independent inputs deactivated, the second inductor voltage is zero, $\hat{v}_{le2} = 0$, so the current through that inductor is zero, $\hat{i}_{le2} = 0$. Since the output voltage is nulled, $\hat{v} = 0$, the load current is also zero $\hat{i} = 0$, and by KCL the inductor current of the first converter must then be zero, $\hat{i}_{\text{le}1} = 0$. There is no current flowing through the first inductor so the voltage drop across it is zero, $\hat{v}_{\text{le}1} = 0$, and, by KVL, the voltage across the first secondary and therefore its primary is zero, $\hat{v}_{\text{pri}1} = 0$. Therefore, the voltage across the extra element port is simply $\hat{v}_{\text{in}} = -e_1\hat{d}_1$ and the current through the extra element port must be $\hat{i}_{\text{in}} = j_1\hat{d}_1$ so that their ratio—the impedance seen at the extra element port—is

$$\boxed{Z_{N1}|_{Z_2=0}^{(1)} = -\frac{e_1}{j_1}} \tag{29}$$

where e_1 and j_1 are linearized model parameters from Fig. 1. Note that inserting canonical model parameters listed in [24] into (29) yields the familiar "negative incremental resistance" for each converter type, e.g., the boost converter presents a null-condition impedance of

$$Z_{N1}|_{Z_2=0}^{(1)} = -\frac{D'^2 V}{I}\left(1 - \frac{sLI}{D'^2 V}\right) \tag{30}$$

a negative impedance at zero frequency. In the equation above, relating to a boost converter, D' is one minus the large signal duty ratio D, V, and I are the large signal output voltage and current respectively, and L is the boost inductor value.

As a distinct example, consider the special-case impedances needed for the interaction parameters, $K_N^{(1)}$ and $K_D^{(1)}$. Note that from (23) and (24), there is some redundancy in the choice of these special-case impedances. Here we derive, $Z_{N1}|_{Z_2=\infty}^{(1)}$ — the null-condition impedance at the first extra element port with the second extra element port open circuited. Because the second port is open circuited, the current through the second primary must be zero, $\hat{i}_{\text{pri}2} = 0$, and so must the current through the second inductor, $\hat{i}_{\text{le}2} = 0$. Since the output voltage is nulled, the rest of the analysis is identical to that for $Z_{N1}|_{Z_2=0}^{(1)}$ and the impedance seen at the extra element port is

$$\boxed{Z_{N1}|_{Z_2=\infty}^{(1)} = -\frac{e_1}{j_1}.} \tag{31}$$

This result is identical to the result for the first special-case impedance. This fact, which is characteristic of the hybrid power system in Fig. 5, simplifies the numerical computation of the correction factors, $\text{CF}^{(i)}$, because the numerator is exactly

factorable as follows:

$$\mathrm{CF}^{(i)} = \frac{\left(1+\frac{Z_1}{Z_{N1}|^{(i)}_{Z_2=0}}\right)\left(1+\frac{Z_2}{Z_{N2}|^{(i)}_{Z_1=0}}\right)}{1+\frac{Z_1}{Z_{D1}|^{(i)}_{Z_2=0}}+\frac{Z_2}{Z_{D2}|^{(i)}_{Z_1=0}}+K_D^{(i)}\frac{Z_1Z_2}{Z_{D1}|^{(i)}_{Z_2=0}\,Z_{D2}|^{(i)}_{Z_1=0}}}. \tag{32}$$

The special-case impedances for correcting the transfer function $\hat{v}/\hat{d}_1$ are summarized here [24]

$$Z_{N1}|^{(1)}_{Z_2=0} = -\frac{e_1}{j_1} \tag{33}$$

$$Z_{N2}|^{(1)}_{Z_1=0} = \frac{Z_{\mathrm{le}2}}{M_2^2} \tag{34}$$

$$Z_{D1}|^{(1)}_{Z_2=0} = \frac{Z_{\mathrm{le}1}+Z_L\|Z_{\mathrm{le}2}}{M_1^2} \tag{35}$$

$$Z_{D2}|^{(1)}_{Z_1=0} = \frac{Z_{\mathrm{le}2}+Z_L\|Z_{\mathrm{le}1}}{M_2^2}. \tag{36}$$

The special-case impedances required to calculate the interaction parameters, $K_N^{(1)}$ and $K_D^{(1)}$, are

$$Z_{N1}|^{(1)}_{Z_2=\infty} = -\frac{e_1}{j_1} \tag{37}$$

$$Z_{D1}|^{(1)}_{Z_2=\infty} = \frac{Z_L+Z_{\mathrm{le}1}}{M_1^2}. \tag{38}$$

In [24], we repeat the calculations above for all of the converter transfer functions in Fig. 4.

V. Design Example: Buffering and Run-Time Integral Diagnostics of a Fuel Cell Under UAV Load Profiles

This section presents a hybrid power system designed for integral fuel cell diagnostics in applications having widely varying load power. The system design goals are suitable fuel cell current buffering, load voltage rejection of impedance spectroscopy activity, and impedance spectroscopy current bandwidth. System performance will be demonstrated under simulated UAV time-domain load profiles. The underlying motivation to diagnose and even heal a damaged fuel cell will be demonstrated experimentally through intentional damaging followed by recovery in conjunction with runtime impedance measurements that support predegradation, postdegradation, and postrecovery conditions of the fuel cell.

The system architecture is a current–voltage regulated hybrid power system like the one analyzed in Section III. Nominal parameters for the two buck converters in the system are shown in Table I. The control signal for generating impedance spectroscopy currents is a perturbation superposed on the fuel cell side converter's reference voltage. The load is modeled as a time-varying current source. The fuel cell is furnished by the current-regulated dc/dc converter, so that the fuel cell operating current may be fixed despite variations in the load current. The battery is furnished by the voltage-regulated dc/dc converter so that it provides the excess load current while constraining the load voltage. The excess load current may be positive or negative so the voltage-regulated converter was designed to support bidirectional current flow. When the excess load current is negative, the battery is inherently recharged by the fuel cell. During impedance spectroscopy, the resulting excess small-signal load current will be largely absorbed by the battery side converter rather than disturbing the load. Effectively, the battery provides the fuel cell impedance spectroscopy current. The feedback control circuitry was designed for good voltage and current regulation, wide bandwidth to support the frequency sweepable impedance spectroscopy current as well as the obvious need for stable closed loop operation. A useful target for the fuel cell impedance spectroscopy current bandwidth was 1 kHz.

TABLE I
Nominal Fuel Cell Power System Parameters

Parameter	Symbol	Value
Fuel cell Voltage	V_{fc}	12 V
Battery Voltage	V_{batt}	12 V
Fuel cell Current	I_{fc}	4 A
Battery Current	I_{batt}	-2 A to $+8$ A
Buck switching freq.	f_{sw}	400 kHz
Buck switching devices	M_i	IRFB3607
Load Voltage	V_o	6 V
Converter Efficiency	η_c	82%

A. Open-Loop and Closed-Loop Dynamics

The usual tradeoffs among phase margin, loop switching frequency attenuation, and bandwidth were addressed using a lead compensator and an additional high frequency pole for both control loops. The loop transfer functions for the implemented system are plotted in Fig. 6 and indicate reasonable phase margin while the loop bandwidth in both plots is wide enough to support sufficiently rich impedance spectroscopy (frequencies up to about 1 kHz). Meanwhile, the loop bandwidths (about 16 kHz) are narrow enough relative to the converter switching frequency (400 kHz) to prevent instability and to mitigate switching ripple in the feedback loop control signals. This design represents a principle tradeoff among loop bandwidth (notably for impedance spectroscopy bandwidth), stability and switching frequency which ultimately impacts converter efficiency.

Closed-loop transfer functions were computed using the analysis from Section II. Some of the key transfer functions are plotted in Fig. 7. Fig. 7(a) shows the fuel cell current response to the control voltage. It shows a bandwidth that is sufficient for the target 1 kHz upper band limit on fuel cell impedance spectroscopy currents. Comparing the responses in Fig. 7(a) and (b) confirm that the control signal needed to achieve suitable excitation currents for the impedance spectroscopy measurements should lead to a relatively small disturbance of the load voltage. Finally, Fig. 7(c) shows the fuel current response to load current perturbations. The plot shows a significant attenuation at low frequency in this regard indicating suitable buffering of the fuel cell current from the variations in the load current. From the discussion in Section II, we know that the low frequency buffering relies on series resistances like inductor ESR in the fuel cell converter's output stage.

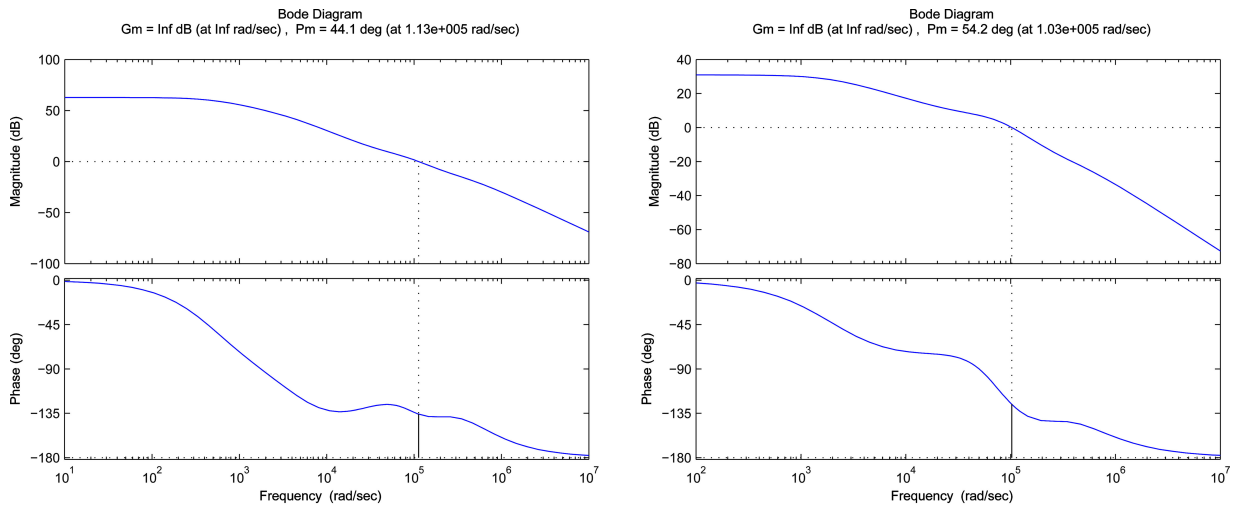

Fig. 6. Open-loop bode plots indicate tradeoffs among loop bandwidth, switching frequency attenuation and stability. (a) Current feedback loop. (b) Voltage feedback loop.

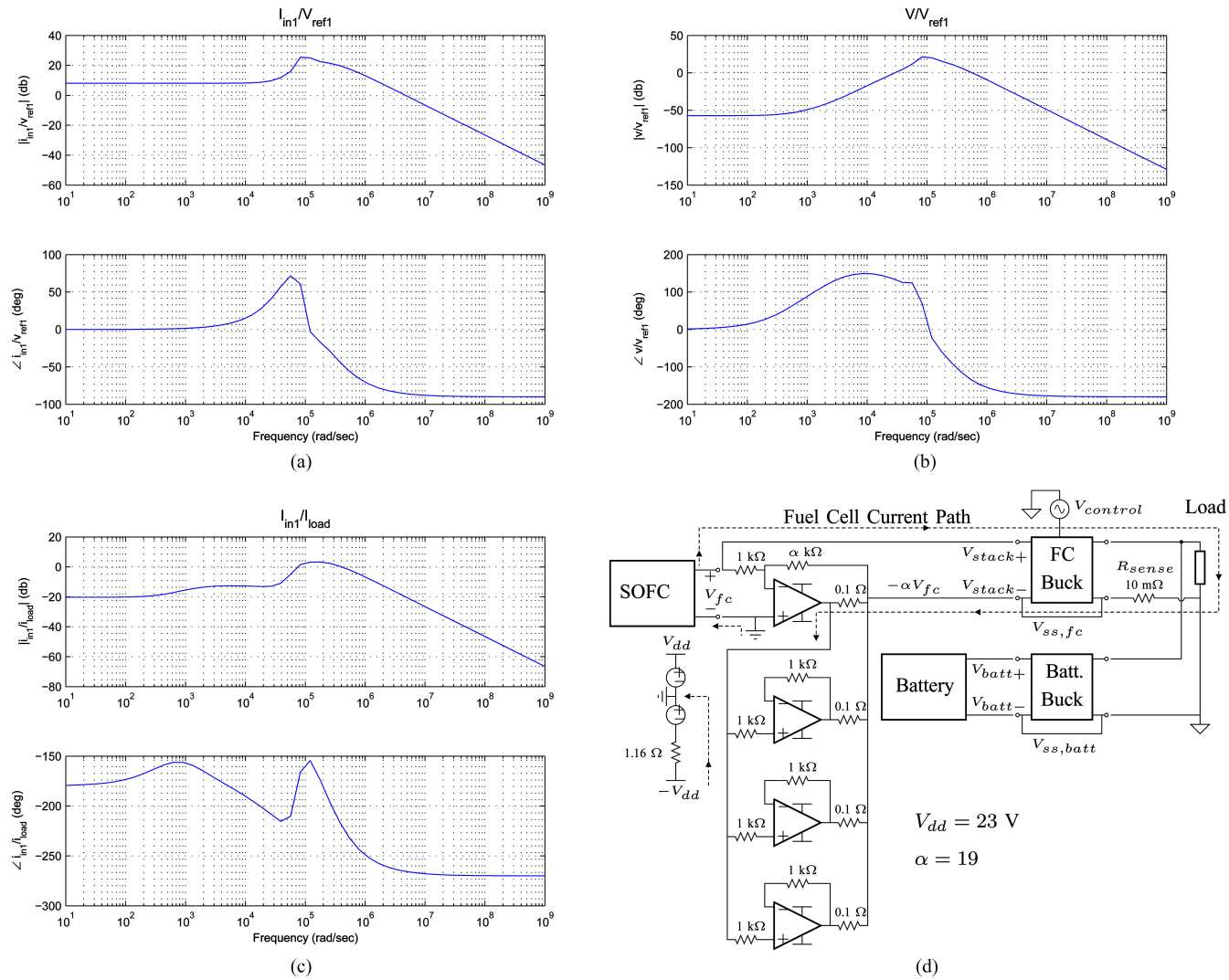

Fig. 7. (a)–(c) Simulated closed-loop bode plots indicate suitable fuel cell current buffering, load voltage rejection of impedance spectroscopy activity, and impedance spectroscopy current bandwidth. (d) Experimental setup block diagram with the Montana State University fuel cell and reference simulator. (a) Control voltage to fuel cell current. (b) Control voltage to load voltage. (c) Load current to fuel cell current. (d) Experimental setup block diagram.

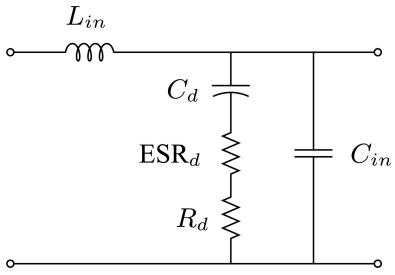

Fig. 8. Common input filter topology.

B. Input Filter

Having designed the system to meet the dynamic requirements for runtime integral diagnostics, input filters were added to attenuate switching frequency content at the fuel cell and battery terminals. The filter on the fuel cell side was chosen not only to attenuate switching ripple, but to pass the impedance spectroscopy current with sufficient bandwidth. The two input filters were designed in concert according to the stability guidelines imposed by the 2EET from Section IV.

The common input filter topology is shown in Fig. 8. The filter elements $L_{\rm in}$ and $C_{\rm in}$ were chosen for good attenuation at the switching frequency. The capacitor C_d was chosen to be very large to represent a low impedance at frequencies near the bandwidth imposed by $L_{\rm in}$ and $C_{\rm in}$. The damping resistor R_d was chosen along with the damping capacitor ESR, to limit peaking in the output impedance of the input filter in order to satisfy the 2EET impedance inequalities from Section IV. Decreasing the value of R_d improves this effect. However, the value of R_d can be optimized to pass impedance spectroscopy currents to the fuel cell and the two input filters need not be the same. There are four correction factors to consider for loop stability—two corresponding to the impact of each input filter on the *current* feedback loop, and two corresponding to the impact of each input filter on the *voltage* feedback loop. Fig. 9 illustrates the tradeoff between the first converter's input filter bandwidth and the negative phase contribution for one of the correction factors. Note that the negative phase contributions indicated by the plotted correction factors are narrowband. That is, they will only impact the stability if the location of the negative phase contribution is very close to the crossover frequency of the corresponding loop transfer function.

A compromise in the value of R_d was chosen for acceptable phase margin and optimized transmission of impedance spectroscopy currents to the fuel cell terminals. Specifically, 200 mΩ was added to the damping capacitor ESR on the fuel cell side yielding an input filter bandwidth of about 1.5 kHz — enough to avoid undermining the closed-loop transfer function bandwidth from the control signal to the fuel cell converter's input current. Because the transmission of impedance spectroscopy current to the battery terminals was less critical in this application (the battery was not the subject of impedance spectroscopy), no resistance was added to the damping resistor on the battery side converter yielding an input filter bandwidth of about 1 kHz. With these input filter choices, the maximum negative phase contribution among all four correction factors was 5°.

C. Experimental Setup

A connection diagram of the experimental setup is shown in Fig. 7(d). The control block diagram corresponding to this system is shown in Fig. 4. Input filters are included in each of the dc–dc converters. The control signal is an ac signal that is added to the dc reference signal on the fuel cell side converter. Cooley in [24] provides circuit level details for the implementation of the reference signal containing both dc and ac components. The experimental setup consists of the two-converter current–voltage-regulated power system, two power sources, and an Agilent N3300A electronic load. The SOFC in this experiment was available through a collaboration with Montana State University (MSU). The fuel cell power source consisted of a subsystem — an electronically simulated fuel cell stack — the reference simulator. This subsystem, shown on the left side of Fig. 7(d), will be described in Section V-D. The second power source was a bidirectional power source, either a lead-acid battery or a bipolar linear power amplifier depending on the particular experiment.

A photograph of the experimental setup is shown in Fig. 10. The power converters and the data acquisition inputs are shown on the left. The measurement, signal generation, and power supplies are shown in the middle of the photo. The fuel cell reference simulator, fuel cell ovens, mass flow and temperature controllers, and fuel bottles are shown on the right. The ovens were heated to a temperature of 750 °C. Electrical terminal were available at the top and bottom of each oven.

D. Reference Simulator

An independent research effort at MSU has led to the successful implementation of a "fuel cell reference simulator." The reference simulator is intended to simulate a series connection (stack) of fuel cells based on the behavior of only one fuel cell. A schematic diagram of the reference simulator in the context of the experimental setup is shown in Fig. 7(d). The reference simulator is effectively presented to the rest of the experimental setup at the terminals labeled $V_{\rm stack+}$ and $V_{\rm stack-}$. It consists of an op-amp gain stage that is reinforced by "slave" op-amp buffers, each one providing unity gain from the output of the op-amp gain stage to the reference simulator output. Each of the op-amp stages comprises a 0.1 Ω current limiting resistor at its output. The emulated fuel cell current flows along the dashed line in Fig. 7(d) — the ground terminals of the op-amps providing a return path to the actual negative terminal of the SOFC cell.

The simulator measures the fuel cell output voltage at $V_{\rm fc}$ and provides a gained and inverted ($-\alpha$) version at the node labeled $V_{\rm stack-}$. The fuel cell voltage is itself included in the simulated stack voltage because the total simulated stack voltage, $V_{\rm stack+} - V_{\rm stack-}$, is

$$\begin{aligned} V_{\rm stack} &= V_{\rm fc} - V_{\rm stack-} \\ &= V_{\rm fc} + \alpha V_{\rm fc}. \end{aligned} \tag{39}$$

The simulated stack voltage is therefore

$$\boxed{V_{\rm stack} = V_{\rm fc}\,(1+\alpha).} \tag{40}$$

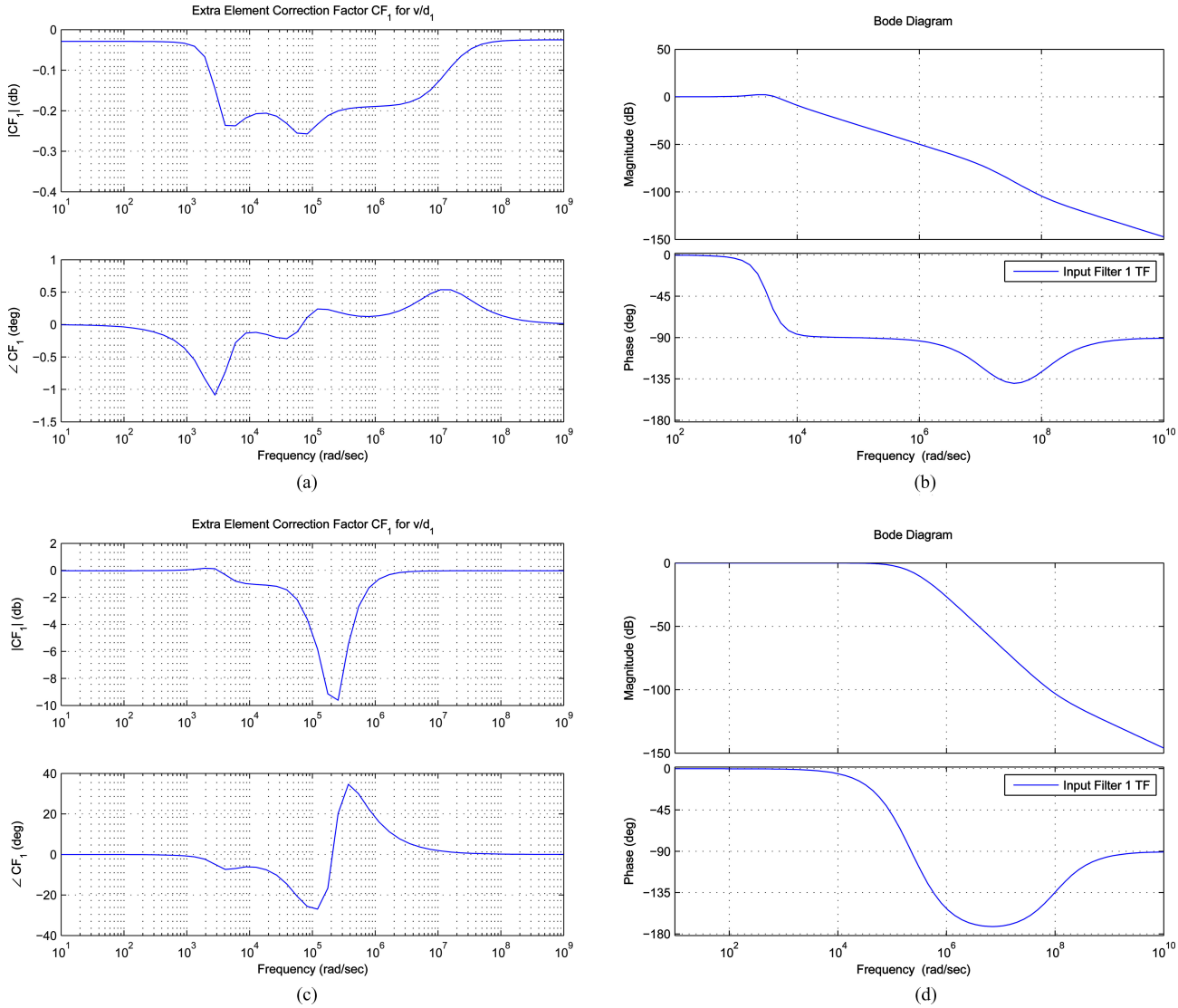

Fig. 9. Plots indicating the tradeoff between input filter negative phase contribution to the loop transfer functions against input filter bandwidth. (a) CF_1, $R_d = 0\ \Omega$. (b) Input filter 1, $R_d = 0\ \Omega$. (c) CF_1, $R_d = 2\ \Omega$. (d) Input filter 1, $R_d = 2\ \Omega$.

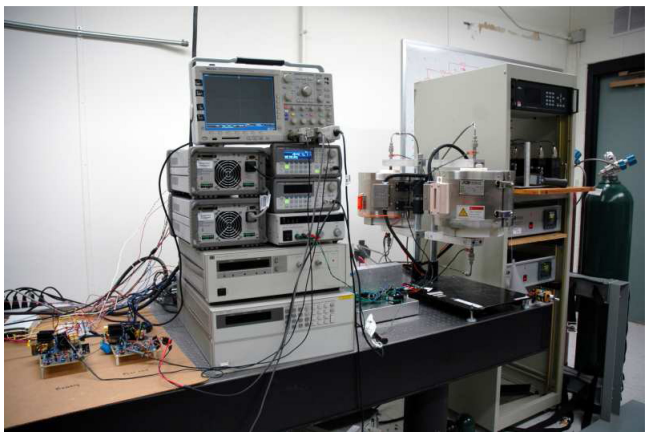

Fig. 10. Photograph of the full experimental setup: (left to right) the data acquisition system, power converters, measurement and power supplies, reference simulator, SOFC ovens mass-flow and temperature controllers, and fuel bottles. Not shown on the left is the 12 V lead-acid battery.

The topology allows the load current to flow through the fuel cell itself. Because all of the fuel cells in a stack would see the same current, the current through the single fuel cell is equivalent to the simulated stack current. Therefore the terminals $V_{\mathrm{stack}+}$ and $V_{\mathrm{stack}-}$ simulate a stack of $1 + \alpha$ replicas of the fuel cell. Additional high power op-amp gain buffers are connected as slave devices to increase the current handling capability of the reference simulator. Note that the reference simulator ground is an intermediate reference that is distinct from the simulated stack reference. The simulated stack reference is generally $V_{\mathrm{stack}-}$ and in this case is connected (through the current sense resistor) to the load ground (load return). The experimental data presented at the end of this section validates the practical use of the hybrid power system for impedance spectroscopy of the fuel cell. It also validates the operation of the reference simulator itself.

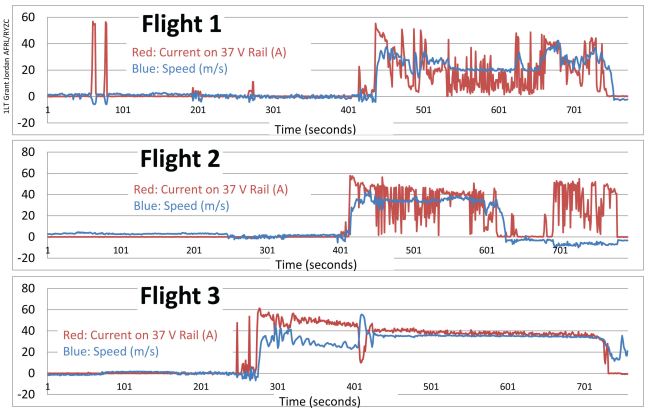

Fig. 11. Data for three different flight plans made available through a collaboration with the USAF. Current is shown in red and aircraft speed is shown in blue.

E. UAV Flight Plans

Electrical flight data for an actual UAV was available through a collaboration with the U.S. Air Force. Data showing the total load current and the UAV velocity time domain profiles (flight plans) are shown for three different flights in Fig. 11. The three different flight plans exhibit some notable and useful features for the run time integral diagnostics experiments. Flight plan 1 exhibits a rapidly and widely varying load current through the flight. Flight plan 2 is similar to flight plan 1 but shows an intermediate landing and takeoff. Flight plan 3 exhibits a slowly varying load current with one distinct abrupt feature near the middle of the flight. Flight plan 3 is particularly useful because it can be used in a simple experiment to determine the extent of the abrupt load transient effects on the impedance spectroscopy measurements.

The oscilloscope traces in Fig. 12 show time domain waveforms about 10 min. long each corresponding to runtime impedance spectroscopy experiments for two different flight plans. The channels in the traces are ch1: battery voltage, ch2: battery current, ch3: fuel cell voltage, ch4: fuel cell current. In the oscilloscope traces, the battery current varies widely throughout the flight plans. When the load current is low, the battery current is actually negative indicating that the battery is being recharged from the fuel cell. The battery voltage varies somewhat due to its internal resistance as the battery current varies with the load. Meanwhile, the fuel cell current and voltage are largely fixed at the desired operating point with a superposed impedance spectroscopy signal. The traces clearly show the frequency-swept impedance spectroscopy signal superposed on the fuel cell current and voltage and the battery current. To a lesser extent, due to the difference in the design of the two input filters described in Section V-B, the impedance spectroscopy signal is visible on the battery current.

In Fig. 12, the EIS sweep is performed twice in succession. The time span of the first sweep includes an abrupt load transient while that of the second sweep does not. This particular dataset may be used to evaluate the effect of the abrupt load transient on the EIS performance. More details can be found in [24].

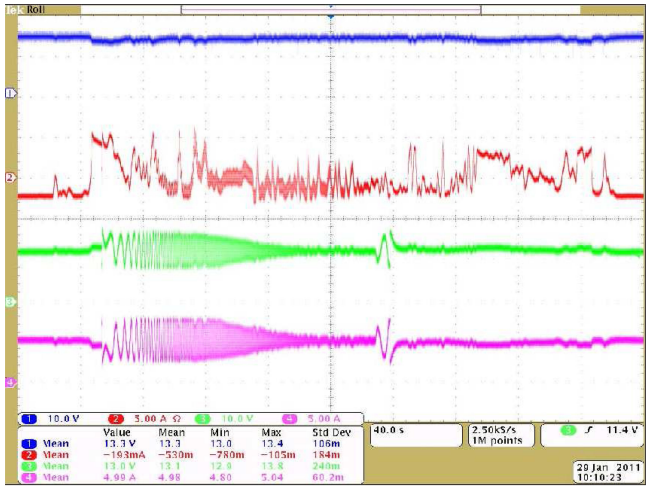

(a)

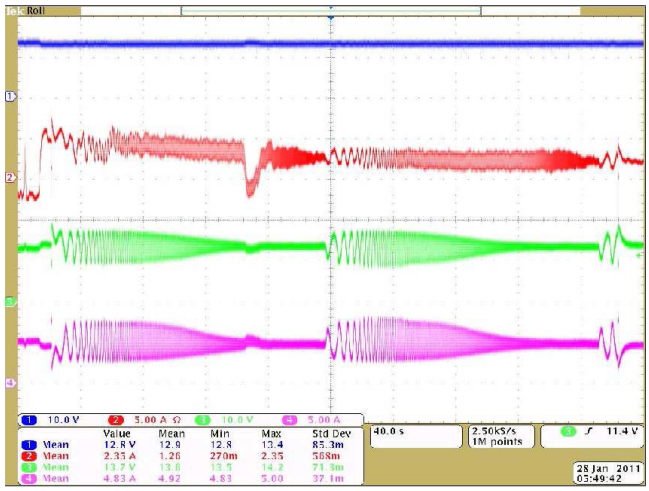

(b)

Fig. 12. Oscilloscope traces showing impedance spectroscopy operation during flight plans (top to bottom), ch1: battery voltage (10 V/div), ch2: battery current (5 A/div), ch3: fuel cell voltage (10 V/div), ch4: fuel cell current (5 A/div). (a) Flight plan 1. (b) Flight plan 3.

F. Fuel Cell Impedance Results

Impedance measurements of the simulated fuel cell stack were taken among various configurations and load profiles. The frequency range of the impedance measurement was 0.1 Hz to 1 kHz. The fuel cell operating point of 4 A was chosen based on its large signal $I-V$ characteristic. The fuel cell impedance was calculated using a time-domain least-squares technique that was presented separately in reference [26].

Fig. 13 shows a comparison of the impedance measured at the single cell level for the two distinct time segments in flight plan 3 at the same fuel cell operating point. The close matching between the two impedance measurements despite the abrupt transient in the load during time segment 1 is a result of the fuel cell current buffering aspect of the power system design.

Fig. 14 shows a comparison of impedance data for a second fuel cell that was intentionally damaged and then allowed to recover. The cell was degraded for about 11 h while holding the cell voltage at 40 mV. The fuel cell current was initially 15 A, but by morning had decreased to 14 A. Fuel rates were

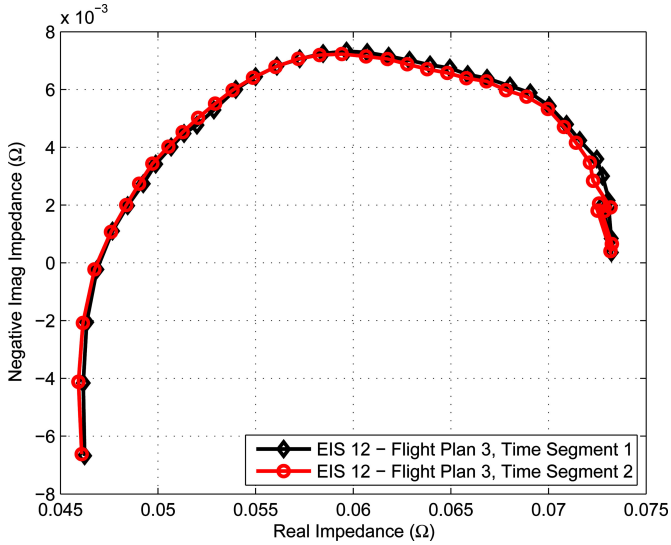

Fig. 13. Single Cell impedance spectroscopy during Flight Plan 3 for two different time segments, $I_{fc} = 4$ A.

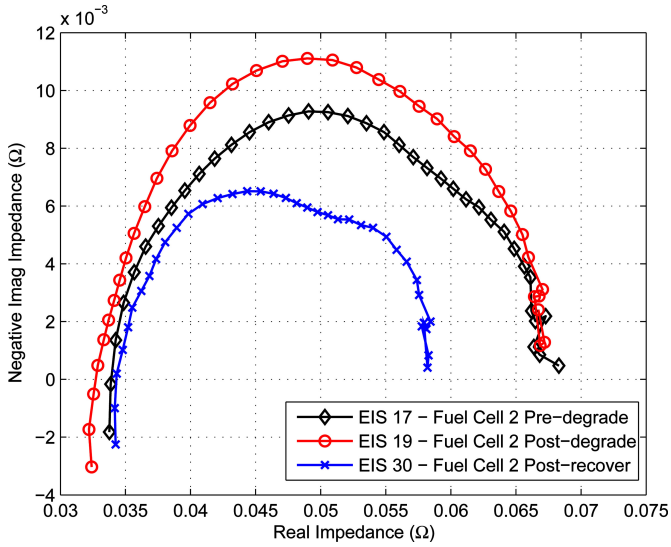

Fig. 14. Predegrade $I_{fc} = 4.1$ A, degraded $I_{fc} = 4$ A, postrecovery $I_{fc} = 4$ A.

260 SCCM H2, 100 SCCM O2. The fuel cell was recovered by leaving it unloaded with the same fuel rates the following night. The cell temperature was 750 °C. The three plots in Fig. 14 correspond to predegradation, postdegradation, and postrecovery. The data suggest that the capacitive impedance increases when the fuel cell has been damaged and decreases when the fuel cell is recovered. The low-frequency resistance (real-axis intercept) also decreases when the fuel cell is recovered. Additionally, the data suggest that the fuel cell was somewhat unhealthy prior to degradation.

The three states of the fuel cell in Fig. 14 may be related to changes in the physical properties of the cell modeled, for instance, by the circuit shown in Fig. 15 from [27]. Some of the elements not included in Fig. 15 are the series inductance leading to the crossing of the real axis in the Nyquist plots and additional *RC* combinations to describe multiple humps in those plots. In the circuit model of Fig. 15, C is the equivalent

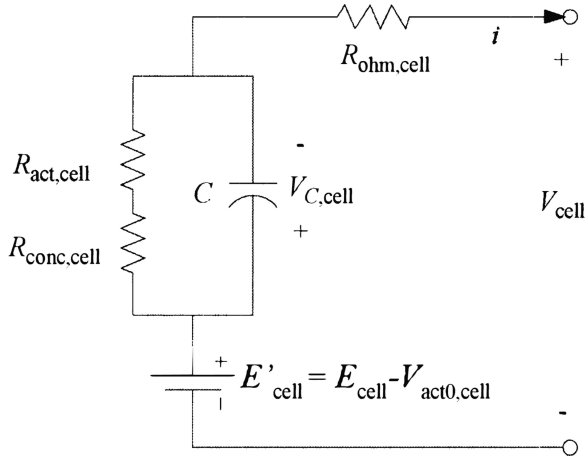

Fig. 15. Circuit model of a solid-oxide fuel cell from [27].

capacitance of the double-layer charge effect at the electrode electrolyte boundary, and $R_{\mathrm{act,cell}}$, $R_{\mathrm{ohm,cell}}$, and $R_{\mathrm{conc,cell}}$ are equivalent resistances of the activation, ohmic and concentration voltage drops. The activation resistance is a representation of the activation energy barrier that must be overcome when chemical reactions start to take place inside the SOFC [27]. The ohmic resistance of the SOFC consists mainly of the resistance of the electrodes, electrolyte, and the interconnection between cells [27]. The concentration drop is a more subtle effect described in detail in [27].

The low-frequency resistance (the real-axis intercept at the right side of the Nyquist plot), would correspond to the series combination of $R_{\mathrm{ohm,cell}} + R_{\mathrm{act,cell}} + R_{\mathrm{conc,cell}}$ because, at low-frequency, the capacitor C can be represented as an open circuit. The high-frequency resistance (the real-axis intercept at the left side of the Nyquist plot), would correspond to the resistance, $R_{\mathrm{ohm,cell}}$ because, at high frequency, the capacitor, C, can be represented as a short circuit. Therefore, the decrease in the low-frequency real-axis intercept indicated by the cell impedance postrecovery would correspond to a decrease in the series combination, $R_{\mathrm{ohm,cell}} + R_{\mathrm{act,cell}} + R_{\mathrm{conc,cell}}$. Meanwhile, the high-frequency resistance, $R_{\mathrm{ohm,cell}}$, has not changed postrecovery, so we may conclude that the series combination $R_{\mathrm{act,cell}} + R_{\mathrm{conc,cell}}$ has decreased in value. This experiment suggests that changes in the low-frequency real-axis intercept representing changes in the activation and concentration drops may be a useful indicator for tracking SOFC health.

1) Fuel Cell Degradation and Recovery Process: The fuel cell is degraded by enforcing near-short circuit conditions on the cell for an extended period of time. This causes a large DC current load drawn from the cell, and a mirroring large oxygen ion flow from the cathode to the anode through the cell's electrolyte. The perceived electrical terminal degradation due to this operation is believed to be caused by nickel oxidation at the anode/electrolyte interface due to a high concentration of diffusing oxygen ions and a low concentration of hydrogen fuel. The oxidation of the nickel, which is included in the anode for catalytic activity and electronic conductivity purposes, results in a decrease in the nickel's catalytic effectiveness and an increase in the anode-side impedance.

To induce recovery from this oxidation, the cell is allowed to operate at open-circuit for several hours while hydrogen and oxygen are still supplied to their respective electrodes at the normal rate. Under these condition, the oxygen ion flow through the electrolyte ceases and allows the reduction of the anode's nickel as the hydrogen concentration increases and accepts the oxygen from the nickel to form water. Further discussion of this sort of degradation and recovery in solid oxide fuel cell's will be published in [28].

VI. Conclusion

This paper has demonstrated run-time extraction of impedance measurements that are useful for identifying and controlling fuel cell health. The power system design focused on aspects for protecting fuel cell health and enabling integral diagnostics including suitable fuel cell current buffering, load voltage rejection of impedance spectroscopy activity, and impedance spectroscopy current bandwidth. The prototype system may benefit electrically propelled UAVs through ruggedized fuel cell power processing based on integral diagnostics and control, while the design process may generally benefit the engineer approaching a multiconverter system design.

References

[1] Z. Zhang, O. Thomsen, and M. Andersen, "Soft-switched dual-input DC–DC converter combining a boost-half-bridge cell and a voltage-fed full-bridge cell," *IEEE Trans. Power Electron.*, vol. 28, no. 11, pp. 4897–4902, Nov. 2013.

[2] J. Cao and A. Emadi, "A new battery/ultracapacitor hybrid energy storage system for electric, hybrid, and plug-in hybrid electric vehicles," *IEEE Trans. Power Electron.*, vol. 27, no. 1, pp. 122–132, Jan. 2012.

[3] O. Hegazy, J. Van Mierlo, and P. Lataire, "Analysis, modeling, and implementation of a multidevice interleaved DC/DC converter for fuel cell hybrid electric vehicles," *IEEE Trans. Power Electron.*, vol. 27, no. 11, pp. 4445–4458, Nov. 2012.

[4] B. Zahedi and L. Norum, "Modeling and simulation of all-electric ships with low-voltage dc hybrid power systems," *IEEE Trans. Power Electron.*, vol. 28, no. 10, pp. 4525–4537, Oct. 2013.

[5] R.-J. Wai, S.-J. Jhung, J.-J. Liaw, and Y.-R. Chang, "Intelligent optimal energy management system for hybrid power sources including fuel cell and battery," *IEEE Trans. Power Electron.*, vol. 28, no. 7, pp. 3231–3244, Jul. 2013.

[6] L. Wang, Z. Wang, and H. Li, "Asymmetrical duty cycle control and decoupled power flow design of a three-port bidirectional DC–DC converter for fuel cell vehicle application," *IEEE Trans. Power Electron.*, vol. 27, no. 2, pp. 891–904, Feb. 2012.

[7] M. Ceraolo, A. Caleo, P. Capozzella, M. Marcacci, L. Carmignani, and A. Pallottini, "A parallel-hybrid drive-train for propulsion of a small scooter," *IEEE Trans. Power Electron.*, vol. 21, no. 3, pp. 768–778, May 2006.

[8] A. Emadi, S. Williamson, and A. Khaligh, "Power electronics intensive solutions for advanced electric, hybrid electric, and fuel cell vehicular power systems," *IEEE Trans. Power Electron.*, vol. 21, no. 3, pp. 567–577, May 2006.

[9] M. Sarhangzadeh, S. Hosseini, M. B. B. Sharifian, and G. Gharehpetian, "Multiinput direct DC/AC converter with high-frequency link for clean power-generation systems," *IEEE Trans. Power Electron.*, vol. 26, no. 6, pp. 1777–1789, Jun. 2011.

[10] W. Jiang and B. Fahimi, "Multiport power electronic interface concept, modeling, and design," *IEEE Trans. Power Electron.*, vol. 26, no. 7, pp. 1890–1900, Jul. 2011.

[11] S. K. Mazumder, K. Acharya, C. L. Haynes, R. Williams, Jr., M. R. v. Spakovsky, D. J. Nelson, D. F. Rancruel, J. Hartvigsen, and R. S. Gemmen, "Solide-oxide-fuel-cell performance and durability: Resolution of the effects of power-conditioning systems and application loads," *IEEE Trans. Power Electron.*, vol. 19, no. 5, pp. 1263–1278, Sep. 2004.

[12] G.-R. Zhu, S.-C. Tan, Y. Chen, and C. Tse, "Mitigation of low-frequency current ripple in fuel-cell inverter systems through waveform control," *IEEE Trans. Power Electron.*, vol. 28, no. 2, pp. 779–792, Feb. 2013.

[13] M. Jang, M. Ciobotaru, and V. Agelidis, "A single-stage fuel cell energy system based on a buck–boost inverter with a backup energy storage unit," *IEEE Trans. Power Electron.*, vol. 27, no. 6, pp. 2825–2834, Jun. 2012.

[14] W.-S. Liu, J.-F. Chen, T.-J. Liang, and R.-L. Lin, "Multicascoded sources for a high-efficiency fuel-cell hybrid power system in high-voltage application," *IEEE Trans. Power Electron.*, vol. 26, no. 3, pp. 931–942, Mar. 2011.

[15] A. Payman, S. Pierfederici, F. Meibody-Tabar, and B. Davat, "An adapted control strategy to minimize dc-bus capacitors of a parallel fuel cell/ultracapacitor hybrid system," *IEEE Trans. Power Electron.*, vol. 26, no. 12, pp. 3843–3852, Dec. 2011.

[16] X. Kong and A. Khambadkone, "Analysis and implementation of a high efficiency, interleaved current-fed full bridge converter for fuel cell system," *IEEE Trans. Power Electron.*, vol. 22, no. 2, pp. 543–550, Mar. 2007.

[17] J. Duarte, M. Hendrix, and M. Simoes, "Three-port bidirectional converter for hybrid fuel cell systems," *IEEE Trans. Power Electron.*, vol. 22, no. 2, pp. 480–487, Mar. 2007.

[18] Z. Jiang, L. Gao, and R. Dougal, "Flexible multiobjective control of power converter in active hybrid fuel cell/battery power sources," *IEEE Trans. Power Electron.*, vol. 20, no. 1, pp. 244–253, Jan. 2005.

[19] V. Thottuvelil and G. Verghese, "Analysis and control design of paralleled DC/DC converters with current sharing," *IEEE Trans. Power Electron.*, vol. 13, no. 4, pp. 635–644, Jul. 1998.

[20] R. Ridley, B. Cho, and F. Lee, "Analysis and interpretation of loop gains of multiloop-controlled switching regulators [power supply circuits]," *IEEE Trans. Power Electron.*, vol. 3, no. 4, pp. 489–498, Oct. 1988.

[21] J. Rajagopalan, K. Xing, Y. Guo, F. Lee, and B. Manners, "Modeling and dynamic analysis of paralleled DC/DC converters with master-slave current sharing control," in *Proc. 11th Annu. Appl. Power Electron. Conf. Expo.*, Mar. 1996, vol. 2, pp. 678–684.

[22] R. Middlebrook and S. Cuk, "A general unified approach to modeling switching-converter power stages," *Int. J. Electron.*, vol. 42, pp. 521–550, Jun. 1977.

[23] R. Middlebrook, "The two extra element theorem," in *Proc. IEEE Front. Educ.*, Sep. 1992, pp. 702–708.

[24] J. J. Cooley, "Analysis, modeling and design of energy management and multisource power systems," Ph.D. dissertation, Massachusetts Inst. Technol., Cambridge, MA, USA, May 2011, ch. 6–9.

[25] R. W. Erickson and D. Maksimovic, *Fundamentals of Power Electronics*, 2nd ed. New York, NY, USA: Springer, 2001.

[26] P. Lindahl, M. Cornachione, and S. Shaw, "A time-domain least squares approach to electrochemical impedance spectroscopy," *IEEE Trans. Instrum. Meas.*, vol. 61, no. 12, pp. 3303–3311, Dec. 2012.

[27] C. Wang and M. Nehrir, "Dynamic modeling and simulation of solid oxide fuel cells," in *Modelling and Control of Fuel Cells; Distributed Generation Applications*, 2009, pp. 85–115.

[28] P. Lindahl, Ph.d. dissertation, Univ. Montana, Bozemann, MT, USA, to be published.

John J. Cooley (S'05–M'11) received the B.S. degree in electrical engineering, the B.S. degree in physics, the M.Eng. degree in electrical engineering, the Electrical Engineer degree, and the Ph.D. degree all from The Massachusetts Institute of Technology, Cambridge, MA, USA, in 2005, 2006, 2007, 2009, and 2011, respectively.

He is currently with FastCAP Systems, Inc., Boston, MA, USA, where he is engaged in the design of power systems for advanced energy storage technologies in automotive and grid-level applications. His research interests include electronics for building energy management and multisource power systems.

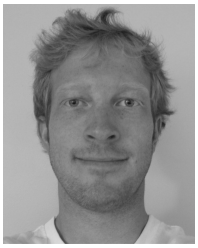

Peter Lindahl (S'08) received the undergraduate degree in electrical engineering from Pennsylvania State University, PA, USA, in 2003, and the Doctoral degree in engineering from Montana State University, Bozeman, MT, USA, in May 2013.

He is currently the CEO and owner of Blackmore Energy, LLC, Bozeman, a company pursuing crowd-sourced solutions for electric grid energy storage. His research interests include energy and power systems, fuel cell systems, renewable energy generation and storage, and energy policy.

Clarissa L. Zimmerman received the B.S. degree in electrical engineering and the M.Eng. degree in 2008 and 2010, respectively, both from the Massachusetts Institute of Technology (MIT), Cambridge, MA, USA, where she built a Nuclear Magnetic Resonance teaching system.

She is currently an Electical Engineering Ph.D. candidate at MIT with a focus on magnetic resonance imaging hardware. Her work on a portable MRI brain scanner is being done at the Martinos Center for Biomedical Imaging.

Matthew Cornachione received the Graduate degree, in 2009, from the Massachusetts Institute of Technology, Cambridge, MA, USA, with a B.S. in physics and a minor in mechanical engineering, the M.S. degree in electrical engineering from Montana State University, Bozeman, MT, USA, in 2011. At Montana State he pursued research involving the degradation and recovery of reversible solid oxide fuel cells.

He is currently an Electrical Engineer for Rocky Mountain Power, Salt Lake City, UT, USA. His research interests include power systems and renewable energy generation.

Grant Jordan received the SB, Electrical Engineering, and Computer Science degrees from the Massachusetts Institue of Technology, Cambridge, MA, USA, in 2007. He is currently working toward the M.S. degree in computer science at UC Sand Diego, La Jolla, CA, USA.

From 2007 to 2011, he was a Developmental Engineer for the Unifted States Air Force.

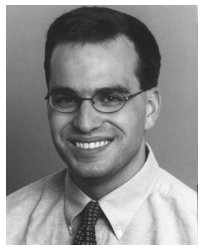

Steven R. Shaw (S'97–M'00–SM'05) received the Doctoral degree from the Massachusetts Institute of Technology, Cambridge, MA, USA, in 2000, in electrical engineering.

He is currently a Professor in the Department of Electrical and Computer Engineering, Montana State University Bozeman, MT, USA. His research interests include system identification and controls, fuel cell systems, instrumentation, and measurement.

Steven B. Leeb (F'07) received the Doctoral degree in electrical engineering and computer science from the Massachusetts Institute of Technology (MIT), Cambridge, MA, USA, in 1993.

He has been with the Department of Electrical Engineering and Computer Science, MIT, since 1993. He is currently a Professor at the Laboratory for Electromagnetic and Electronic Systems, MIT, where he is engaged in the design, analysis, development, and maintenance processes for all kinds of machinery with electrical actuators, sensors, or power electronic drives.